Paleosecular variation record from Pleistocene-Holocene lava flows in southern Colombia

Wellington P. de Oliveira [a,*], Gelvam A. Hartmann [a], Jairo F. Savian [b], Giovanny Nova [c], Mauricio Parra [c], Andrew J. Biggin [d], Ricardo I.F. Trindade [e]

[a] Instituto de Geociências, Universidade Estadual de Campinas, Rua Carlos Gomes 250, 13083-855, Campinas, SP, Brazil
[b] Instituto de Geociências, Universidade Federal do Rio Grande do Sul, Av. Bento Gonçalves 9500, 91501-970, Porto Alegre, RS, Brazil
[c] Instituto de Geociências, Universidade de São Paulo, Rua do Lago 562, 05508-080, São Paulo, SP, Brazil
[d] Department of Earth, Ocean and Ecological Science, University of Liverpool, Liverpool L69 7ZE, UK
[e] Departamento de Geofísica, Instituto de Astronomia, Geofísica e Ciências Atmosféricas, Universidade de São Paulo, Rua do Matão 1226, 05508-900, São Paulo, SP, Brazil

ARTICLE INFO

ABSTRACT

Improvements in the spatial and temporal coverage of paleomagnetic data are essential to better evaluate paleofield behaviour over the past 10 Myr, especially due to data scarcity at low latitudes in the South American region. Here, we provide new Pleistocene-Holocene (0–2 Ma age interval) paleodirectional data from three volcanic systems (Doña Juana Volcanic Complex, Galeras Volcanic Complex and Morasurco Volcano) in southwestern Colombia between latitudes 1.2 and 1.4°N. A total of 38 paleodirectional sites were studied using progressive alternating field and thermal demagnetization treatments. After excluding transitional data, we obtain thirty site-mean directions for analysis of paleosecular variation (PSV) and the time-averaged field (TAF) in the study area. The mean direction (Dec = 351.2°, Inc = −3.4°, α_{95} = 6.2°, k = 20.0) and the paleomagnetic pole (Plat = 80.7°N, Plon = 173.1°E, A_{95} = 5.2°, K = 29.1) of these sites are not statistically compatible with the expected geocentric axial dipole (GAD) field direction and geographic north pole, respectively. Virtual geomagnetic pole dispersion (S_B) for our filtered dataset ($S_{B(2Ma)} = 15.2^{17.6°}_{12.0}$) and the Brunhes chron ($S_{B(Bru)} = 16.0^{19.1°}_{11.6}$) are consistent at the 95% confidence level with South American studies at equatorial latitudes and recent PSV models for the 0–10 Ma and Brunhes intervals. Likewise, the corresponding inclination anomaly (ΔI) for two age groups $\Delta I_{2Ma} = -5.9^{0.3°}_{12.1}$ and $\Delta I_{Bru} = -5.3^{3.1°}_{13.7}$ suggests large deviations relative to the GAD model, in accordance with predictions from zonal TAF models. The high VGP dispersion could be linked to strong longitudinal variability of the magnetic equator position over South America. This feature reflects the presence of significant non-dipole field components in this region that have been detected in geomagnetic field models for the most recent centuries and millennia, probably associated with the presence of the South Atlantic Magnetic Anomaly in the South American region.

1. Introduction

Earth's magnetic field has a dominantly internal origin and varies both in direction and intensity over a wide range of timescales. Investigations into paleosecular variation (PSV), which is manifest as long-period (10^5–10^6 years) geomagnetic variations (Johnson and McFadden, 2015), provide valuable information about geomagnetic field evolution and constrain numerical geodynamo simulations (Coe and Glatzmaier, 2006; Lhuillier et al., 2013; Davies and Constable, 2014; Sprain et al., 2019; Biggin et al., 2020). When PSV is averaged over a long interval,

the time-averaged field (TAF) can be represented to first approximation by a geocentric axial dipole (GAD; Merrill and McFadden, 2003). This assumption is central to paleomagnetism with applications for plate tectonic reconstructions (Tauxe, 2003).

Geological records from volcanic rocks are considered highly appropriate for determining the statistical properties of paleofield behaviour over the past few million years. These materials offer instantaneous readings of the paleomagnetic field in contrast to the smoothed recording in sedimentary rocks (Hulot et al., 2010). Over the past 14 years, global compilations of high-quality paleomagnetic data

---

* Corresponding author.
  E-mail address: weloliveira@ige.unicamp.br (W.P. de Oliveira).

(from lava flows and thin dykes) have been produced for the last 5 Myr (Johnson et al., 2008; Opdyke et al., 2015) and 10 Myr (Cromwell et al., 2018) to constrain PSV and TAF models. de Oliveira et al. (2021) presented an updated 0–10 Ma database that improves the geographic and temporal coverage of paleodirectional data compared to previous compilations.

A statistic commonly employed to quantify PSV is the angular dispersion of virtual geomagnetic poles (VGPs) for a certain location. Several PSV models (e.g., Constable and Parker, 1988; Tauxe and Kent, 2004; Bono et al., 2020; Brandt et al., 2020) have been developed to describe the latitudinal dependence of PSV based on spherical harmonic analyses fitted to VGP dispersion data. Model G (McFadden et al., 1988) assumes that overall dispersion can be described by separating two independent families. These are primary and secondary families, respectively, associated with asymmetrical (e.g., axial dipole) and symmetrical (e.g., axial quadrupole) harmonic terms about the equator. This model has been employed widely in evaluations of PSV behaviour over

Phanerozoic timescales (e.g., Biggin et al., 2008; Veikkolainen and Pesonen, 2014; de Oliveira et al., 2018; Doubrovine et al., 2019; Franco et al., 2019; Handford et al., 2021) and provides important insights into geomagnetic field stability. For the 0–10 Ma period, strong latitudinal variation of the VGP dispersion curve has been reported in two studies (Cromwell et al., 2018; de Oliveira et al., 2021), although small differences were observed in the Model G curves mainly due to the methods used to calculate the VGP dispersion. The data selection of de Oliveira et al. (2021) includes a minimum of 10 paleomagnetic sites per selected study and at least 5 samples per site, which differs from a previous compilation (Cromwell et al., 2018).

Insights can also be gained into paleomagnetic field morphology from PSV studies. Statistical analysis of the latitudinal pattern of inclination anomaly data spanning the last 10 Myr enables TAF models (Bono et al., 2020; de Oliveira et al., 2021) to suggest the existence of axial quadrupole and octupole contributions <5% of the axial dipole term. The presence of small non-GAD terms appears similar to
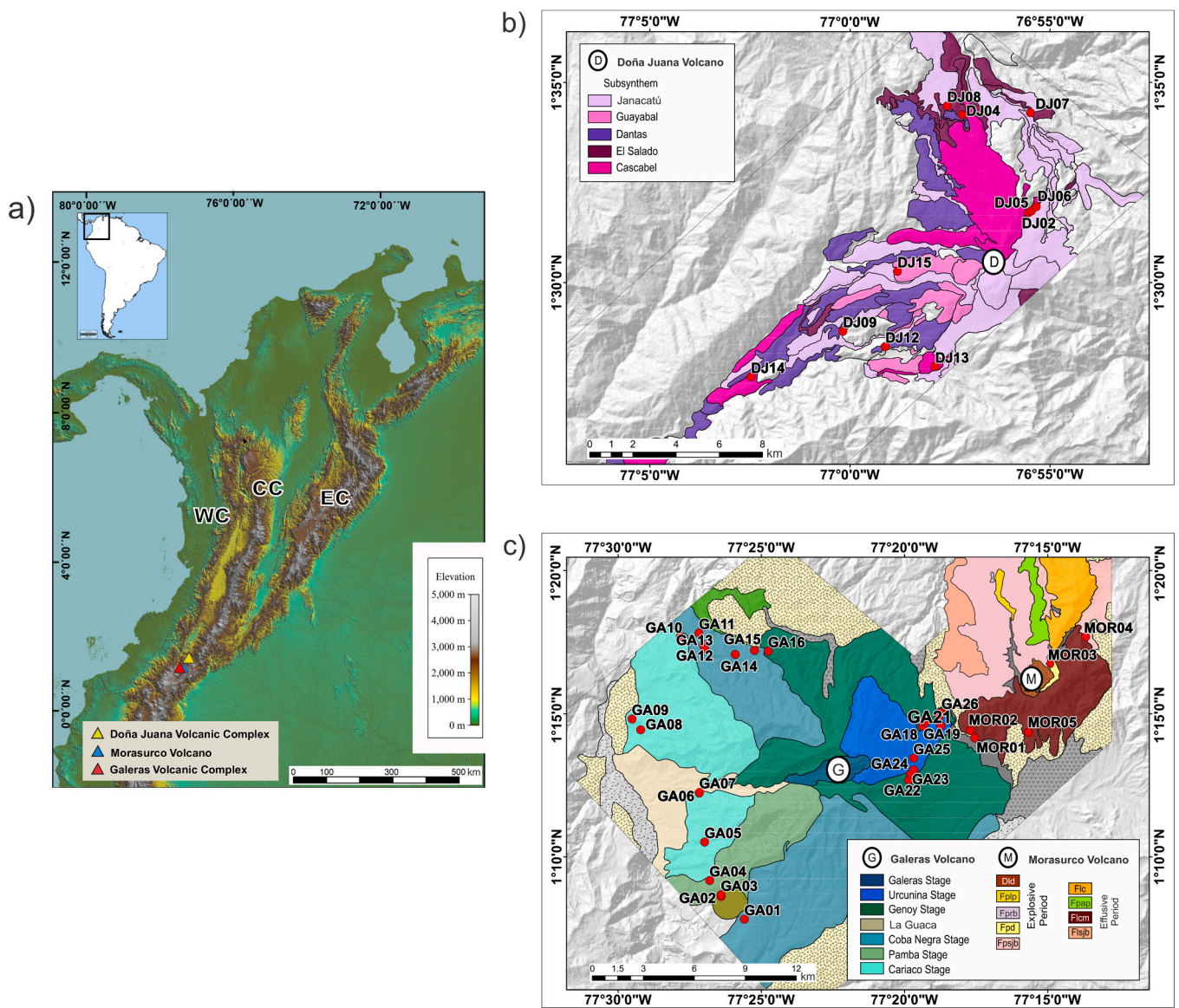
Fig. 1. (a) Topographic map of Colombia (WC: Western Cordillera; CC: Central Cordillera; EC: Eastern Cordillera) with the location of the three studied volcanic systems. Geologic maps of (b) Doña Juana Volcanic Complex, and (c) Morasurco Volcano and Galeras Volcanic Complex. Red circles indicate paleomagnetic site locations. Modified from Pardo et al. (2019), Duque Trujillo et al. (2010), and Calvache et al. (1997). (For interpretation of the references to colour in this figure legend, the reader is referred to the web version of this article.)

geomagnetic field models for the 0–5 Ma (McElhinny et al., 1996; Johnson et al., 2008) and 0–100 ka intervals (Panovska et al., 2018). However, the detailed structure of average paleomagnetic field reconstructions is limited by the non-uniform spatial and temporal distributions of paleodirectional data. In particular, South America contributes only 10% of the current 0–10 Ma database (de Oliveira et al., 2021). There are also few PSV studies at low latitudes (e.g., Leonhardt et al., 2003; Opdyke et al., 2006; Sánchez-Duque et al., 2016), which is a region with negative inclination anomalies ($> -2°$) associated with a persistent zonal quadrupole component. Therefore, acquisition of new paleomagnetic records is essential to better assess the latitudinal TAF structure and long-term geomagnetic variations.

In this study, we present high-quality paleodirectional data from Pleistocene-Holocene lava flows from the southwestern region of Colombia's Northern Volcanic Zone (NVZ) at latitudes of 1.2°-1.4°N. Additionally, we provide reliable estimates of VGP dispersion and inclination anomaly from a careful selection of site-level data. These results are compared with low latitude paleomagnetic data to assess the validity of recent PSV and TAF models for the 0–10 Ma interval.

2. Geologic setting

The present morphology of Colombia's NVZ originated from subduction and collision of Pacific-related plates, including the Farallon, Nazca, and Caribbean plates beneath or against the South American plate, respectively (Taboada et al., 2000; Wagner et al., 2017; Montes et al., 2019). These interactions triggered uplift of the Northern Andes (extending from Colombia to the Ecuador), which in Colombia is divided into three mountain ranges, the Western, Central and Eastern Cordilleras (Fig. 1a). One of the main geological features is the Romeral Fault System (RFS), which delimits oceanic crustal basement of the Western Cordillera from continental basement of the intermontane Cauca Valley to the east in the Central Cordillera. The eastern side of the RFS consists of medium-grade metamorphic Triassic-Jurassic rocks (Spikings et al., 2015), a Triassic sedimentary succession (Mojica, 1980; Cediel et al., 1981) and Jurassic intrusive bodies (e.g., Ibague Batholith, Sombrerillo Batholith, Mariquita Stock) (Cochrane et al., 2014; Bustamante et al., 2016; Zapata et al., 2016; Rodríguez et al., 2018), and volcano-sedimentary sequences (Bayona et al., 1994; Mojica and Prinz-Grimm, 2000; Bayona et al., 2020). To the west, the NVZ is composed of Cretaceous low-grade metamorphic belts and oceanic mafic rocks (Quebradagrande and Arquia Complexes) related to the Caribbean Large Igneous Province (McCourt et al., 1984; Kerr et al., 1996; Pindell and Kennan, 2009; Villagómez et al., 2011), and including Cenozoic granodioritic plutons (Jaramillo et al., 2017; Zapata et al., 2019).

Over the NVZ basement, a series of volcanoes was built along the Central Cordillera as a result of magmatic and tectonic activity from the western continental margin of Colombia since the Miocene (Ramos, 2009; Monsalve Bustamante, 2020). The present study focuses on three stratovolcanoes located in the southwest Colombian Andes (1.2–1.4°N, 76.9–77.4°W; Fig. 1a): the Doña Juana Volcanic Complex (DJVC), Morasurco Volcano, and Galeras Volcanic Complex (GVC). These stratovolcanoes are mainly composed of dacite and andesite lava flows with calc-alkaline affinity interlayered with pyroclastic deposits, associated with effusive and explosive events that occurred over the last 2.5 Myr (Monsalve Bustamante, 2020). A general description of the geologic units of each volcano is given below.

The DJVC contains several types of volcanic deposits such as pyroclastic flows, lava flows and ash beds with ages ranging from 1125.4 ± 4.4 ka to the present-day, supported by $^{40}Ar/^{39}Ar$ and ^{14}C datings (Pardo et al., 2019). These authors defined five unconformity-bounded lithostratigraphic units, referred to as subsynthems, based on structural angular unconformities and include lithosomes (defined for eruptive centers) in the volcanic area as follows (Fig. 1b). (1) The Cascabel Subsynthem corresponds to the oldest volcanic deposits (between 1125.4 ± 4.4 ka and 1097 ± 39 ka) that overlap the Cretaceous

metamorphic basement. It comprises dacitic and andesite lava flows of the Santa Helena Lithosome, and includes ignimbrites, lahar deposits and porphyritic dacites from the Animas Lithosome. (2) The El Salado Subsynthem, which consists of lava dome, welded ignimbrite, lahar and lapilli tuff deposits of the Animas Lithosome emplaced from 1097 ka to 878 ka. (3) The Dantas Subsynthem is composed of massive ash-flow deposits and andesitic to dacitic lava flows related to the Ancestral Doña Juana Lithosome, with ages ranging between 878 ± 2.8 ka and 312 ± 28.8 ka. (4) The Guayabal Subsynthem (from 230.8 ± 13.3 ka to 76.8 ± 18 ka) comprises ignimbrites and dacitic lava flows from the Old Doña Juana Lithosome, massive tuffs from the Animas Lithosome and debris-avalanche deposits from the Montoso Lithosome. (5) The Janacatú Subsynthem represents the youngest volcanic deposits, consisting of block-ash flows and lahars from the Young Doña Juana Lithosome, pyroclastic deposits and ignimbrites from the Animas Lithosome, and lahar and hyperconcentrated flow deposits from the Totoral Lithosome. Its period of volcanic activity is dated between 4400 ± 30 yrs BP and 1936 CE.

The Morasurco Volcano is considered inactive and is located to the southwest of the DJVC (Fig. 1c) with volcanic deposits dated to 1.6–2.2 Ma based on zircon fission-track and K/Ar methods (Duque Trujillo et al., 2010). The authors recognized five lava flow units and four pyroclastic flows associated with two eruptive phases. The first phase corresponds to an effusive event with a large volume of basaltic andesite lava flows distributed around the volcanic center and include the San Juan Bajo lava flow (Flsjb), undifferentiated Cerro Morasurco lava flow (Flcm), Alto de Piedras lava flow (Flap) and Loma La Cocha lava flow (Flc). A subsequent event is restricted to explosive activity, characterized by deformation of the volcanic edifice, which is partially destroyed and comprises pyroclastic deposits named the San Juan Bajo pyroclastic flow (Fpsjb), Daza pyroclastic flow (Fpd), Río Bermúdez pyroclastic flow (Fprb), Quebrada Las Palmas pyroclastic flow (Fplp) and Daza Lava Dome (Dld).

The Galeras Volcano (Fig. 1c) is regarded as the most active volcano in Colombia (Calvache and Duque-Trujillo, 2016), and can be divided stratigraphically into six Late Pleistocene-Holocene geologic stages (Calvache et al., 1997). The oldest volcanic materials belong to the Cariaco stage, which is composed of lava or dome collapse flows, andesite lavas and ash and blocks of pyroclastic flow deposits dated at 1.1 ± 0.1 Ma (K-Ar; Cepeda, 1985). The subsequent products of explosive eruption of the Pamba stage (1.1–0.793 Ma) consist of partially welded block and ash flow deposits. This episode is succeeded by the Coba Negra stage, which consists of andesitic to basaltic and occasionally dacitic lava flows deposited over 793–288 ka ($^{40}Ar/^{39}Ar$). La Guaca (166 ± 34 ka; $^{40}Ar/^{39}Ar$) is designated as a monogenetic cinder cone on the southwestern part of the GVC. Its deposits are mainly composed of olivine-bearing basaltic andesites. Explosive eruptions followed during the Genoy stage that produced pyroclastic deposits with ages between 159 ± 21 ka ($^{40}Ar/^{39}Ar$) and 41 ± 1.5 ka (^{14}C). The next episode occurred during the Urcunina stage, characterized by andesite lava flows with pyroclastic flows in the age range from 41 ± 1.5 to 12.8 ± 0.3 ka (^{14}C). The youngest stage, termed Galeras, is situated in the center of the GVC. The volcanic products consist of pyroclastic flows, pyroclastic falls, mud and debris flows with ^{14}C ages covering the last 4500 years.

3. Sampling

A total of 42 paleomagnetic sites were sampled in southern Colombia during June 2019 (Figs. 1 and 2) at altitudes between 1404 and 3289 m. a.s.l. (meters above sea level). Eleven sites were sampled in the DJVC and twenty-six and five sites were sampled from the Galeras and Morasurco volcanoes, respectively. All volcanic sites correspond to individual Pleistocene to Holocene lava flows (predominantly andesites) from different geological formations within the study area (Calvache et al., 1997; Duque Trujillo et al., 2010; Pardo et al., 2019). Most of the

Fig. 2. Fieldwork images of the paleomagnetic sites sampled. (a) Site DJ08 (Doña Juana Volcano), (b) site MOR04 (Morasurco Volcano) with core sample drill holes (below), and (c) sites GA17 and GA21 (Galeras Volcano).

paleomagnetic targets were accessed by paved roads and tracks around the three stratovolcanoes, but long hikes were made to access some lava outcrops. All sampling sites appeared unaltered. Site coordinates were obtained with a portable global positioning system device. An average of 9 core samples 2.5 cm in diameter and ~ 10 cm in length were collected at each site with a handheld gasoline-powered drill. Cores were oriented with a magnetic compass. It was not possible to obtain sun compass measurements due to cloud cover. It is worth noting that the natural remanent magnetization (NRM) intensities (Table S1) of the samples are low (<1 A/m) in order not to affect the magnetic compass needle.

4. Methods

4.1. Paleodirectional experiments

All paleomagnetic experiments were carried out in the Paleomagnetism Laboratory at the University of São Paulo (USPMag). For paleo-direction measurements, oriented samples were sliced into 1.2 cm-long specimens and were subjected to stepwise thermal demagnetization (THD) and alternating-field demagnetization (AFD) procedures in a magnetically shielded room. THD was performed using an ASC Scientific Model TD48 oven. Magnetic measurements and AFD were made using a 2G Enterprises cryogenic magnetometer equipped with a RAPID (Rock and Paleomagnetism Instrument Development) system. At least five

specimens from each site (577 specimens in total) were subjected to AFD (393 specimens) in 18 steps up to 100 mT or using THD treatment (184 specimens) in 15 steps from room temperature to 600 °C. From measurements of pilot specimens (two specimens per site), AFD was employed in preference to THD because the latter yielded noisy data or magnetizations decreased rapidly during the first demagnetization steps

for most pilot specimens.

4.2. Data analysis procedures

Characteristic remanent magnetization (ChRM) directions from individual specimens were determined using principal component
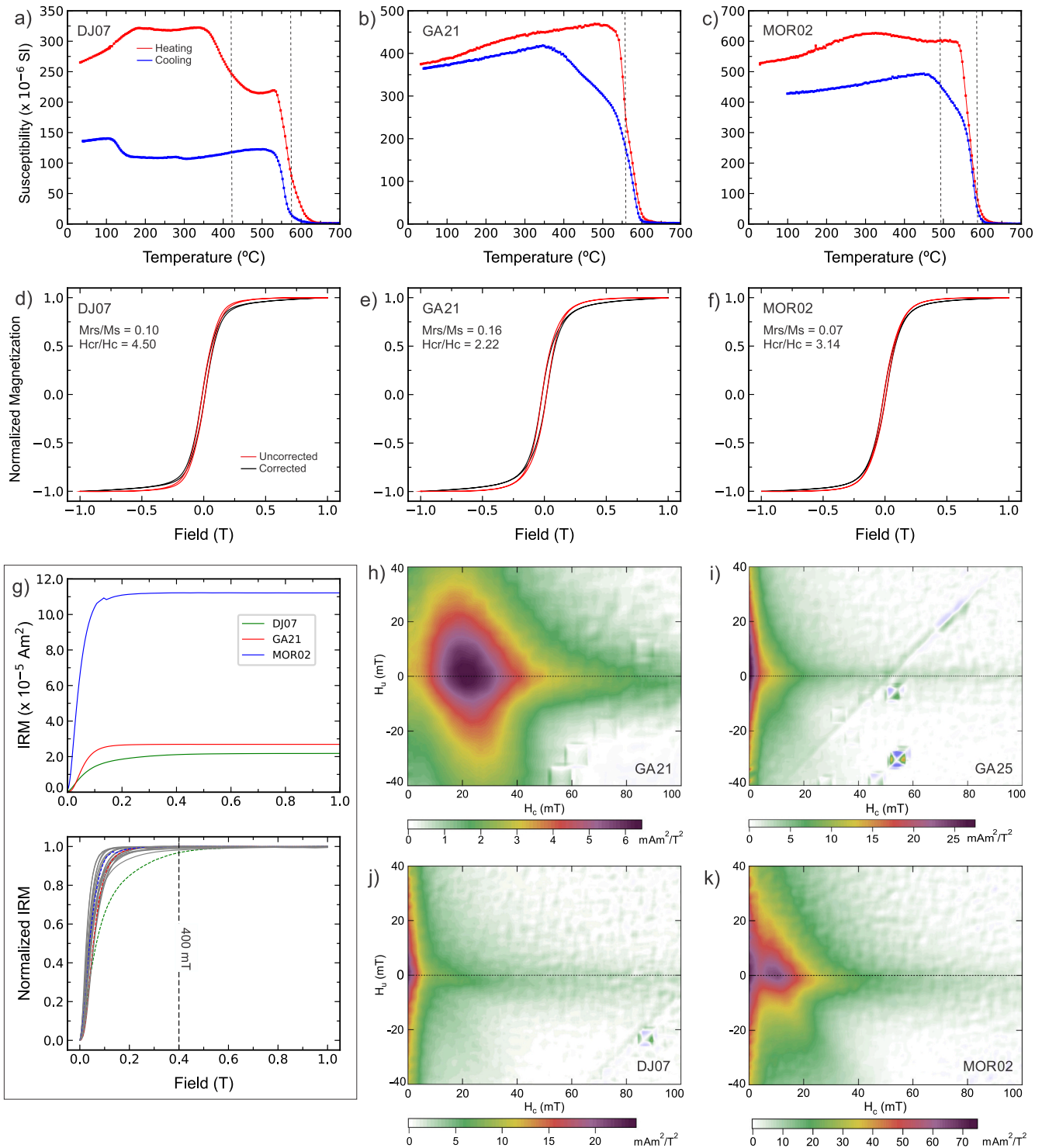

Fig. 3. Rock magnetic results for representative samples. (a-c) Thermomagnetic curves with heating (red curve) and cooling (blue curve) cycles. Dashed lines indicate the magnetic transition temperatures. (d-f) Normalized hysteresis loops, where red curves are not corrected for high field slopes. (g) IRM acquisition curves for 3 sites (top) and normalized IRM results for 21 sites (bottom). (h-k) FORC diagrams with magnetic domain structures for (h) vortex, (i-j) multidomain (MD), and (k) a mixture of vortex state and MD grains. IRM = isothermal remanent magnetization; FORC = first-order reversal curve. (For interpretation of the references to colour in this figure legend, the reader is referred to the web version of this article.)

analysis (Kirschvink, 1980). Data from at least six consecutive demagnetization steps represented in Zijderveld diagrams (Zijderveld, 1967) were used for ChRM estimation, as long as directions trended toward to the origin of the Zijderveld diagram and have a maximum angular deviation (MAD) $\leq$ 5°. Site-mean directions were calculated using an approximate uncertainty propagation for specimen ChRM directions (Table S1) proposed by Heslop and Roberts (2020), which is applied to Fisher (1953) distributed data. Similar to the criterion used by de Oliveira et al. (2021), we considered at least five specimens per site ($n \geq 5$) with precision parameter (Banerjee et al., 2005) values of $k \geq 50$. Furthermore, the paleomagnetic results were evaluated applying the Vandamme (1994) criterion, which allows identification of excursional sites and outlier data that could be possibly related to the self-reversed thermoremanent magnetizations (TRMs), as reported in andesite rocks from the northern Colombian Andes (Heller et al., 1986; Haag et al., 1990). We do not use a fixed 45° cutoff for VGP data because it could lead to overestimation (underestimation) of VGP scatter for low and high latitudes (Franco et al., 2019; de Oliveira et al., 2021).

4.3. Magnetic mineralogy measurements

Rock magnetic experiments were performed on one sample per site (from 21 representative sites) to examine thermal stability during heating-cooling cycles in magnetic susceptibility measurements, and to determine the magnetic carriers and their magnetic domain states. Thermomagnetic susceptibility $\chi(T)$ curves were measured for crushed samples with a KLY4 Kappabridge susceptibility meter coupled to a CS-3 furnace (AGICO). Heating cycles were measured from 30 °C to 700 °C (at 12 °C/min) in air with subsequent cooling to 40 °C. The Curie temperatures (T_C) of all samples were determined from the second derivative approach (Tauxe, 2003), which have been used also for $\chi(T)$ curves (e.g., Gautam et al., 2004; Salminen and Pesonen, 2007; Aldana et al., 2011). From a single small rock fragment per site, hysteresis loops, isothermal remanent magnetization (IRM) acquisition curves, and first-order reversal curves (FORCs) were measured using a Princeton Measurements vibrating sample magnetometer (VSM) MicroMag 3900, with its maximum applied fields at room temperature. The hysteresis parameters, saturation magnetization (M_s), saturation remanence magnetization (M_{rs}), coercive force (H_c) and coercivity of remanence (H_{cr}) were used to investigate the domain structures of magnetic minerals. Plotting these parameters on a Day diagram (Day et al., 1977) is unsuitable for identifying multiple magnetic components (Roberts et al., 2018), so FORC diagrams (Roberts et al., 2000) allow better assessment of mineralogical composition and magnetic domain states in mixed magnetic particle systems (Roberts et al., 2014; Zhao et al., 2017). FORC measurements were made with an averaging time of 100 ms; 200 FORCs were measured. All FORC data were processed using the FORCinel software (Harrison and Feinberg, 2008) with a smoothing factor of 5.

5. Results

5.1. Rock magnetism

The selected samples have variable thermomagnetic curves (Fig. 3a-c; Fig. S1) with up to two magnetic transition temperatures inferred using the maximum in the second derivatives for the heating curves. About 52% of samples have a single ferrimagnetic phase with high transition temperatures of 516–594 °C (Fig. 3b, Table S2), which suggest the presence of Ti-poor titanomagnetite, pure magnetite or maghemite (Dunlop and Özdemir, 1997; Evans and Heller, 2003). Other samples contain two magnetic phases with Curie temperatures between 189 and 603 °C (see Table S2), which indicate the presence of titanomagnetite with different Ti contents (Evans and Heller, 2003; Lattard et al., 2006). In particular, samples DJ07 and MOR02 (Fig. 3a and c) have, respectively, a secondary transition temperature at 421 °C and 497 °C (associated with a hump shaped behaviour in the heating curves), which

could be attributed to the presence of oxidized titanomagnetite or titanomaghemite (Dunlop and Özdemir, 1997). In general, the heating-cooling curves are irreversible with higher magnetic susceptibility during the heating cycle than during cooling. Non-reversible behaviour indicates alteration of magnetic minerals during measurement.

Hysteresis loops are narrow (Fig. 3d-f and Fig. S2) with low coercivity $H_c < 20$ mT (Table S2) and a small paramagnetic mineral fraction. IRM curves saturate in fields from 0.15 to 0.4 T (Fig. 3g), which suggests a major contribution from low-coercivity minerals. These results are typical of magnetite, titanomagnetite, and partially oxidized magnetite and titanomaghemite (Dunlop and Özdemir, 1997). A Day plot (Day et al., 1977) is provided in Fig. S3.

From FORC diagrams, we identify two magnetic domain patterns (Fig. 3h-k). The first reveals the existence of vortex state particles (Roberts et al., 2017; Lascu et al., 2018; Egli, 2021), which are characterized by moderate elongation over the vertical (H_u) axis and H_c values below 60 mT, with strong vertical spreading due to vortex nucleation (Fig. 3h). Another FORC configuration indicates the presence of multidomain (MD) grains with a large spread of outer contours along the H_u axis and a H_c peak below 10 mT (Fig. 3i-j). Some samples have two contributions with a mixture of vortex and MD particles, as shown in Fig. 3k. FORC diagrams for other paleomagnetic sites are presented in Fig. S4.

5.2. Paleodirection

ChRM components were determined for 38 paleomagnetic sites using both AFD and THD. Only four sites (DJ09, DJ12, DJ14, and GA06) failed to produce acceptable results because of highly scattered data. Examples of representative demagnetization diagrams (Zijderveld plots) are shown in Fig. 4. In general, NRM directions are well grouped, with ChRM directions defined by the best-fit line for data that converge to the origin of the plots after removal of viscous components with AFD >5 mT (Fig. 4a and c) or > 200 °C (Fig. 4b and d). AFD and THD yield similar results for specimens measured at the same site (e.g., Fig. 4e-f).

Our dataset comprises 36 site-mean directions (summarized in Table 1) that satisfy the selection criterion described in section 4.2. For further TAF and PSV analysis, we discarded 6 out of 36 sites that are considered to record transitional directions by applying the Vandamme (1994) criterion (Fig. 5a). Among these, 21 sites have normal polarity and 9 have reversed polarity. The normal and reversed polarity directions pass a bootstrap reversals test (Tauxe, 2010) within the 95% confidence region (Fig. S5), which allows calculation of the mean direction by combining these two groups of sites. Furthermore, our dataset ($N = 30$ sites) passes the quantile-quantile (Q-Q) test (Fisher et al., 1987) at the 95% confidence level, with statistical parameters $M_u = 1.190$ and $M_e = 0.462$ below critical values $M_u' = 1.207$ and $M_e' = 1.094$, respectively (Tauxe, 2010) (Fig. S6). This fact supports the hypothesis that declination and inclination data are distributed uniformly and exponentially, respectively. After converting reversed polarity data to normal polarity, the overall mean direction for N = 30 sites is declination (D) = 351.2°, inclination (I) = −3.4°, and 95% confidence cone (α_{95}) = 6.2°, which includes uncertainty propagation (Heslop and Roberts, 2020). This result is statistically distinguishable at the 95% confidence level with the predicted direction for a GAD field ($D_{GAD} = 0°$, $I_{GAD} = 2.54°$) at the mean latitude (1.27°N) of the sampling region (Table 2 and Fig. 5a).

VGPs were calculated from the paleolocations and mean directions for all sites (Table 1). Site paleolocations were determined using the NNR-MORVEL 56 plate motion model (Argus et al., 2011) to correct for plate tectonic movements. The paleomagnetic pole was calculated from the filtered dataset by averaging the site-level VGPs, considering the antipodes of the reversed polarity sites and VGP uncertainties. Our mean paleomagnetic pole (latitude = 80.7°N, longitude = 173.1°E, $A_{95} = 5.2°$) does not coincide at the 95% confidence interval with Earth's spin axis (Table 2). The VGP positions and the paleopole are shown in the
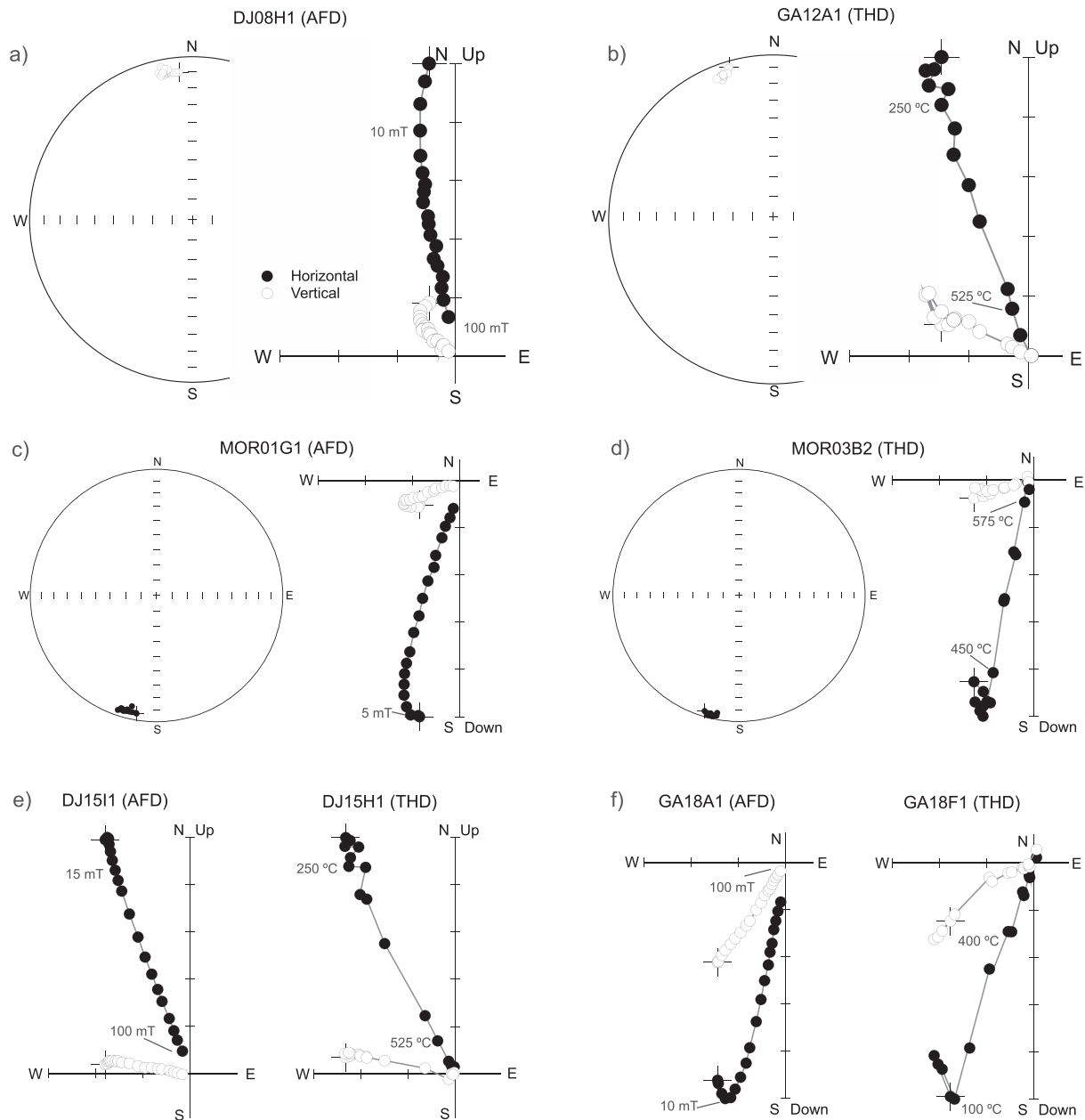
Fig. 4. Examples of demagnetization diagrams. Zijderveld diagrams and stereographic projections of NRM components obtained during (a and c) alternating field demagnetization (AFD) and (b and d) thermal demagnetization (THD). (e-f) Orthogonal projections of sister specimens using two demagnetization methods. Filled (open) circles correspond to vector components in the horizontal (vertical) plane for Zijderveld projections and upper (lower) hemisphere for stereographic projections. NRM = natural remanent magnetization.

polar projection map in Fig. 5b.

6. Discussion

6.1. Magnetic polarity of the sampled sites

Based on geochronological studies in the studied area (e.g., Calvache et al., 1997; Duque Trujillo et al., 2010; Pardo et al., 2019), the entire dataset (including excursional sites) covers an age interval of 0–2.0 Ma, and spans the Brunhes (0–0.78 Ma) and Matuyama (0.78–2.58 Ma) chrons. Information about ages with references for the studied paleomagnetic sites are presented in Table 1. Considering the age range assigned to each site (and age uncertainties), the magnetic polarity of the paleodirectional sites is approximately consistent with the expected polarity of geologic polarity time scale 2020 (GPTS2020; Ogg, 2020), as

shown in Fig. 6. Four sites (GA17, GA18, GA19, and GA23) for the 159–31 ka age interval record reversed polarity (maybe induced by a self-reversed TRM) within the Brunhes normal chron. These sites probably record one of several young short-lived reversed polarity events (Laj and Channell, 2015), such as the Mono Lake (33 ka), Laschamp (41 ka), or Blake (120 ka) excursions. Moreover, our dataset spans at least six paleomagnetic reversals, which represents a period long enough (~2 Ma) to record and average paleosecular variation.

6.2. VGP dispersion estimates

To evaluate geomagnetic paleosecular variation in the study region, the angular dispersion of VGP distributions relative to the mean paleopole was calculated as the between-site dispersion (S_B) that removes random errors associated with within-site VGP dispersion (S_w),

Table 1
Summary of paleodirectional results.

Site	Altitude (m)	Slat (°N)	Slon (°E)	Slat* (°N)	Slon* (°E)	n/N	Demag	Dec (°)	Inc (°)	α95 (°)	k	Vlat (°N)	Vlon (°E)	A95 (°)	Pol	Age (Ma)	Ref
DJ02	3101	1.529	283.074	1.470	283.129	7/16	AF	222.5	54.6	6.1	114.9	−36.0	240.4	4.3	T	1.125–1.112	1
DJ04	2348	1.570	283.047	1.518	283.096	9/11	AF + Th	189.6	−16.7	3.0	333.1	−78.2	156.3	1.8	R	1.097–0.878	1
DJ05	3120	1.530	283.076	1.471	283.131	9/14	AF + Th	148.3	−7.2	5.6	95.4	−58.2	17.6	4.2	R	1.125–1.112	1
DJ06	3027	1.532	283.078	1.473	283.133	7/12	AF	119.0	−8.3	10.0	44.2	−29.0	17.1	4.8	T	1.125–1.112	1
DJ07	2557	1.571	283.075	1.519	283.124	10/16	Th	355.8	−15.3	4.1	153.7	79.8	126.8	3.2	N	1.097–0.878	1
DJ08	2541	1.574	283.040	1.522	283.089	10/11	AF	347.7	−6.3	3.8	185.4	76.9	172.2	2.2	N	1.097–0.878	1
DJ09	2287	1.478	282.997	1.484	283.003	0/5	AF	–	–	–	–	–	–	–	–	0.00321–0.00303	1
DJ12	2482	1.479	283.015	1.467	283.034	0/5	AF	–	–	–	–	–	–	–	–	0.312 ± 0.029	1
DJ13	2809	1.465	283.035	1.407	283.089	7/11	AF + Th	358.3	−6.1	9.2	52.0	85.2	123.8	8.3	N	1.097 ± 0.039	1
DJ14	1404	1.461	282.959	1.401	283.014	0/5	AF	–	–	–	–	–	–	–	–	~1.125	1
DJ15	2757	1.505	283.020	1.507	283.029	11/16	AF + Th	344.8	−1.9	5.0	92.7	74.6	183.9	4.6	N	0.0804 ± 0.0019	1
GA01	2405	1.131	282.574	1.098	282.609	13/14	AF + Th	344.8	7.2	5.0	76.2	74.6	202.4	4.1	N	0.793–0.560	2
GA02	2230	1.144	282.561	1.141	282.574	12/16	AF + Th	2.0	2.2	3.9	139.2	88.0	13.9	3.1	N	0.166 ± 0.034	2
GA03	2238	1.145	282.561	1.142	282.574	13/16	AF + Th	356.2	−8.4	2.4	319.2	83.4	137.8	1.9	N	0.166 ± 0.034	2
GA04	2047	1.153	282.554	1.104	282.601	7/15	AF	326.1	47.1	9.3	50.6	47.3	235.9	7.0	T	0.793–1.1	2
GA05	1785	1.175	282.551	1.117	282.605	11/16	AF	220.9	−23.0	3.5	190.9	−48.0	175.8	2.6	T	1.1 ± 0.1	2
GA06	1672	1.204	282.547	1.146	282.601	0/7	Th	–	–	–	–	–	–	–	–	1.1 ± 0.1	2
GA07	1678	1.204	282.547	1.146	282.601	12/16	Th	151.2	71.9	5.3	75.1	−27.2	299.6	5.4	T	1.1 ± 0.1	2
GA08	1727	1.241	282.513	1.184	282.567	6/12	AF + Th	219.3	11.4	10.2	53.1	−50.1	203.1	7.9	T	1.1 ± 0.1	2
GA09	1675	1.247	282.508	1.190	282.562	11/14	AF + Th	210.0	81.1	7.1	47.4	−13.1	273.7	11.4	T	1.1 ± 0.1	2
GA10	1769	1.295	282.536	1.237	282.590	5/14	AF + Th	349.1	5.2	12.0	52.3	79.1	199.9	9.2	N	1.1 ± 0.1	2
GA11	1872	1.297	282.547	1.264	282.582	13/16	AF + Th	339.6	−10.0	4.2	104.8	68.7	175.2	2.1	N	0.793–0.560	2
GA12	1930	1.290	282.550	1.257	282.585	12/15	Th	339.0	−5.2	2.8	261.2	68.7	182.1	1.0	N	0.793–0.560	2
GA13	1972	1.288	282.550	1.255	282.585	7/12	AF + Th	5.4	20.0	7.8	72.1	79.5	312.0	5.4	N	0.793–0.560	2
GA14	2209	1.284	282.568	1.251	282.603	6/11	AF + Th	345.4	−7.6	7.1	108.1	74.6	173.3	5.8	N	0.793–0.560	2
GA15	2317	1.287	282.579	1.254	282.614	11/14	AF + Th	7.3	−12.0	3.4	195.1	79.7	58.1	2.2	N	0.793–0.560	2
GA16	2246	1.286	282.587	1.287	282.597	12/14	AF + Th	8.8	5.8	5.1	80.8	81.1	1.9	3.1	N	0.159–0.031	2
GA17	2647	1.243	282.678	1.244	282.688	11/12	AF + Th	183.0	20.8	3.9	155.1	−77.6	268.6	3.1	R	0.159–0.031	2
GA18	2639	1.245	282.679	1.246	282.689	14/14	AF + Th	191.9	18.1	4.2	100.2	−74.1	234.6	3.0	R	0.159–0.031	2
GA19	2640	1.246	282.678	1.247	282.688	14/16	AF + Th	169.2	−10.6	3.7	122.5	−78.5	33.8	2.2	R	0.159–0.031	2
GA20	2585	1.248	282.687	1.254	282.693	6/12	AF + Th	320.8	−1.1	5.8	163.0	50.8	190.3	2.8	N	0.012 ± 0.0015	2
GA21	2608	1.243	282.688	1.249	282.694	10/15	AF + Th	15.2	−2.1	6.6	60.3	74.6	21.3	5.0	N	0.012 ± 0.0015	2
GA22	3282	1.211	282.669	1.212	282.679	11/14	AF + Th	354.9	−19.7	5.3	82.2	77.5	126.6	2.8	N	0.159–0.031	2
GA23	3250	1.215	282.670	1.216	282.680	8/16	AF + Th	211.7	−17.3	7.1	71.1	−57.6	178.0	4.2	T	0.159–0.031	2
GA24	3211	1.217	282.672	1.223	282.678	12/20	AF + Th	334.7	−3.0	2.9	243.2	64.5	186.6	2.1	N	0.012 ± 0.0015	2
GA25	3132	1.224	282.672	1.230	282.678	10/14	AF + Th	330.5	−8.1	4.5	127.7	60.0	182.3	3.2	N	0.012 ± 0.0015	2
GA26	2472	1.251	282.688	1.252	282.698	13/15	AF + Th	340.8	1.1	4.6	88.0	70.8	191.0	2.8	N	0.159–0.031	2
MOR01	2547	1.236	282.708	1.139	282.791	8/13	AF	182.8	−8.1	7.0	73.0	−86.0	145.2	5.5	R	1.95–1.60	3
MOR02	2636	1.240	282.705	1.143	282.788	10/15	AF	161.6	43.6	6.3	66.6	−58.0	314.7	6.2	R	1.95–1.60	3
MOR03	2847	1.279	282.751	1.182	282.834	18/24	AF + Th	178.1	3.5	3.2	124.2	−86.5	315.9	2.5	R	1.95–1.60	3
MOR04	2749	1.295	282.772	1.183	282.866	9/19	AF	169.8	−2.5	7.8	50.1	−79.9	13.3	4.5	R	2.015 ± 0.268	3
MOR05	2808	1.239	282.739	1.128	282.833	9/14	AF	342.2	5.9	6.5	72.1	72.1	199.0	5.0	N	2.015 ± 0.268	3

Site is the site name (DJ = Doña Juana Volcano; MOR = Morasurco Volcano; GA = Galeras Volcano); Slat and Slon are the latitude and longitude of the paleomagnetic site; Slat* and Slon* correspond to the site paleolatitude and paleolongitude determined using the NNR-MORVEL56 plate motion model (Argus et al., 2011); n is the number of specimens used to calculate site-mean directions (see Table S1); N is the total number of specimens processed for each site; Demag refers to the demagnetization method used: thermal (Th) or alternating field (AF) demagnetization; Dec and Inc. are mean site declination and inclination, respectively; α_{95} is the 95% confidence cone around the site-mean direction; k is the parameter precision of directions approximated (Banerjee et al., 2005); Vlat and Vlon are the latitude and longitude of the virtual geomagnetic poles (VGPs) calculated from site paleolocations; A_{95} is the 95% confidence cone around the site-mean VGP. Pol is the geomagnetic polarity: normal (N), reversed (R), and transitional (T) directions; age represents the age interval assigned to each site based on geochronological studies; Ref denotes Reference ID: 1. Pardo et al. (2019); 2. Calvache et al. (1997); 3. Duque Trujillo et al. (2010).
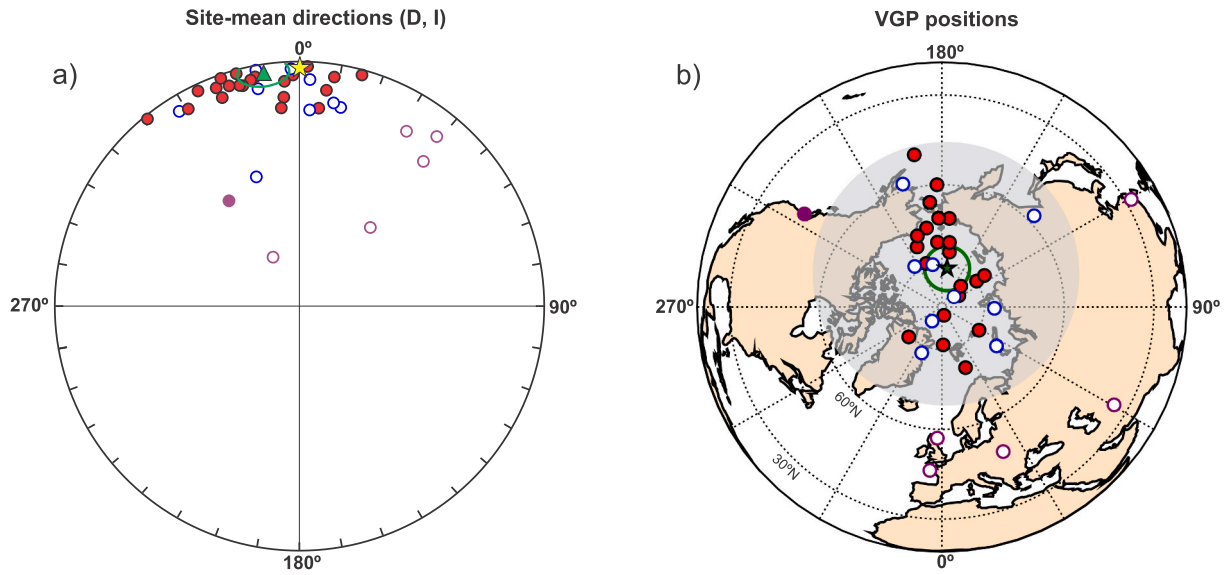
Fig. 5. Equal area projection of site-mean directions for the filtered dataset ($N = 30$ sites). (a) Filled red (open blue) circles represent normal (and antipodes of reverses) polarity directions. Green triangle represents the mean inclination with its 95% confidence circle (green circle). The yellow star is the expected GAD direction. Purple circles indicate transitional data based on the Vandamme (1994) criterion and were not used for PSV and TAF analysis. (b) Polar stereographic map of VGP positions. Closed (open) circles correspond to normal (reversed) polarity site VGPs projected onto the Northern Hemisphere. The green star indicates the paleopole position with its 95% confidence circle (green circle). Data for transitional sites (purple circles) that were removed after applying the Vandamme (1994) cutoff (32.6°) are outside the transparent grey circle. GAD = geocentric axial dipole; VGP = virtual geomagnetic pole. (For interpretation of the references to colour in this figure legend, the reader is referred to the web version of this article.)

Table 2
Statistical results of the mean paleodirection for the two age groups.

Age (Ma)	Slat (°N)	Slon (°E)	N	D (°)	I (°)	k	α_{95} (°)	ΔI (°)	Plat (°N)	Plon (°E)	K	A_{95} (°)	S_B (°)	S_{Bl} (°)	S_B^u (°)
0–2.02	1.27	282.76	30	351.2	−3.4	20.0	6.2	−5.9	80.7	173.1	29.1	5.2	15.2	12.0	17.6
Brunhes	1.24	282.65	16	349.3	−2.8	22.2	8.4	−5.3	79.0	178.8	27.4	7.5	16.0	11.6	19.1

Age is age interval of site groups; Slat and Slon are the mean site latitude and longitude; N is the number of sites; D and I are mean declination and inclination; k and α_{95} indicate the parameter precision approximated (Banerjee et al., 2005) and 95% confidence cone about the mean direction; ΔI is inclination anomaly estimate; Plat and Plon are the latitude and longitude of the mean VGP; K and A_{95} indicate the parameter precision approximated (Banerjee et al., 2005) and 95% confidence cone about the mean VGP; S_B is the between-site VGP dispersion; S_{Bl} and S_B^u are the lower and upper 95% confidence limits of S_B.

expressed by (Biggin et al., 2008):

$$S_B = \sqrt{\frac{1}{N-1}\sum_{i=1}^{N}\left(\Delta_i^2 - \frac{S_{wi}^2}{n_i}\right)}, \tag{1}$$

where N is the total number of sites, and Δ_i corresponds to the angular distance between the ith VGP and the paleomagnetic pole. The within-site dispersion is given by:

$$S_{wi} = \frac{81}{\sqrt{K_i}}, \tag{2}$$

where K_i is the Fisher precision parameter for each VGP determined from direction space (k_i) and the site paleolatitude (λ_i), following Cox (1970):

$$K_i = \frac{8k_i}{5 + 18sin^2\lambda_i + 9sin^4\lambda_i}. \tag{3}$$

From the filtered dataset, we calculated the dispersion S_B and the 95% bootstrap confidence limits (Efron and Tibshirani, 1993) for the 0–2 Ma age interval and Brunhes normal polarity data (Table 2). The Matuyama reversed chron was not considered here due to the small data quantity ($N = 6$ sites), which is unlikely to produce an adequate PSV estimate (Biggin et al., 2008; Johnson et al., 2008). The VGP dispersion estimated $S_{B(2Ma)} = 15.2_{12.0}^{17.6°}$ (with lower (S_{Bl}) and upper (S_B^u) 95% confidence

limits) for the 0–2 Ma period is statistically compatible to the Brunhes chron data with $S_{B(Bru)} = 16.0_{11.6}^{19.1°}$ (16 sites). These estimates are compared to the latitudinal distribution of global S_B data (grey circles), along with PSV models (Model G of McFadden et al. (1988)) proposed by de Oliveira et al. (2021) for the 0–10 Ma and Brunhes intervals (Fig. 7a and b, respectively). We use the PSV models based on the upgraded 0–10 Ma database with the Vandamme (1994) criterion applied (de Oliveira et al., 2021). As shown in Fig. 7a-b, $S_{B(2Ma)}$ and $S_{B(Bru)}$ estimates presented here (red squares) have higher values relative to the 0–10 Ma (7 studies) and Brunhes (4 studies) data within the −10° to 10° latitudinal range. However, these estimates are not significantly different at the 95% confidence intervals from the results of most other PSV studies (see Table 3). Additionally, our results coincide with VGP dispersion values predicted by Model G ($S_B = 12.4_{10.9}^{13.7°}$ for the 0–10 Ma period and $S_B = 11.2_{9.5}^{13.0°}$ for the Brunhes chron) within the 95% uncertainty limits (brown dashed curve).

The high VGP dispersion documented here for the study area may be linked to the enhanced longitudinal variability of the magnetic equator in the Atlantic sector (30° to 90°W). In this region, a higher level of PSV activity has been detected compared to the Pacific sector from present-day, centennial (Panovska and Constable, 2017), and millennial scale geomagnetic field models (Constable et al., 2016; Panovska et al., 2019) and in numerical geodynamo models (Aubert et al., 2013; Terra-Nova et al., 2019). The strongest magnetic equator fluctuations in the Atlantic region could be caused by the South Atlantic Anomaly (SAA), which is a
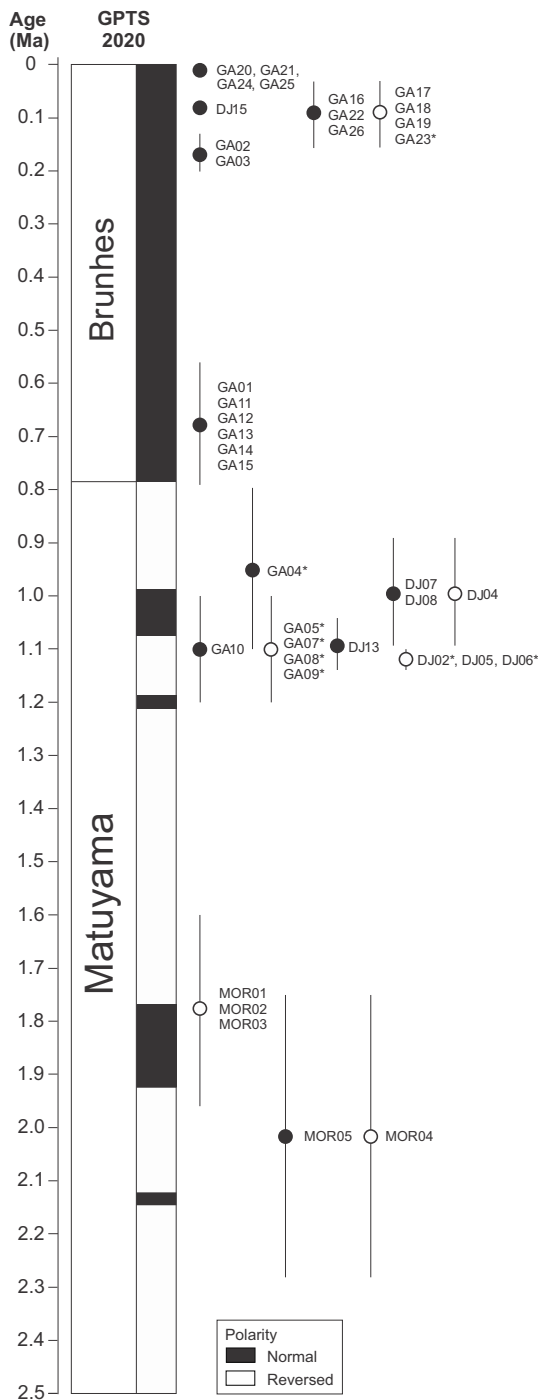
Fig. 6. Magnetic polarity of the paleomagnetic sites from this study compared to the geomagnetic polarity time scale (GPTS2020) of Ogg (2020). Black (white) circles denote normal (reversed) polarity. The age range attributed to the studied sites is represented by a vertical line supported by geochronological studies (see Table 1). *Transitional sites identified using the Vandamme (1994) criterion.

zone of weak field intensity located between southern Africa and South America (e.g., Hartmann and Pacca, 2009) large westward declination, and complex spatial inclination behaviour (Rother et al., 2021). Some studies (e.g., Tarduno et al., 2015; Engbers et al., 2022) suggest the longevity of this feature over million-year timescales. It seems possible that the high VGP scatter found in southern Colombia is due to paleomagnetic field direction changes near the magnetic equator. There is only other one dataset for latitude 0.5°S (Opdyke et al., 2006) with $S_B =$

$12.5_{10.5}^{14.5°}$ from the 0–10 Ma database (Table 3). Therefore, further investigations are needed in the South American equatorial region to address paleomagnetic data scarcity in this area.

6.3. Time-averaged inclination anomalies

A statistical approach usually employed to describe directional deviations from a GAD field refers to the inclination anomaly (ΔI), which is defined as the difference between observed inclination (I_{OBS}) and the GAD inclination, following Cox (1975):

$$\Delta I = I_{OBS} - I_{GAD}. \tag{4}$$

Using Eq. (4), an inclination anomaly for two age groups (0–2 Ma and Brunhes chron datasets) was calculated from the mean inclination (Fisher, 1953) minus the expected GAD inclination (I_{GAD}). The latter is determined as a function of the mean latitude (λ) for site groups:

$$I_{GAD} = tan^{-1}(2tan\lambda). \tag{5}$$

Accordingly, inclination anomaly estimates are $\Delta I_{2Ma} = -5.9_{-12.1}^{0.3°}$ for the 0–2.0 Ma interval and $\Delta I_{Bru} = -5.3_{-13.7}^{3.1°}$ for the Brunhes normal polarity chron. These values are statistically indistinguishable from one other and from the GAD field model ($\Delta I = 0°$) within 95% confidence limits (Table 2). For comparative purposes, the corresponding estimates are shown in Fig. 7c and d, together with global ΔI data as a function of latitude (excluding site-level directions using the Vandamme (1994) cutoff method) with respect to zonal TAF model of de Oliveira et al. (2021) over the 0–10 Ma and Brunhes chron periods. These models are suggestive for the presence of minor non-dipole field components that are defined by axial quadrupole contributions of 3.2% and 2.0% (for the 0–10 Ma and Brunhes intervals, respectively) relative to the axial dipole term, with smaller axial octupole contributions of about 1.2%. As can be seen in Fig. 7c-d, our inclination anomaly data (red triangles) are statistically compatible with paleomagnetic studies located along the $-10°$ to $10°$ latitude band (Table 3) and predictions of TAF models within 95% confidence regions (blue shaded areas). Thus, the negative inclination anomalies observed at equatorial latitudes (including ours) are consistent with zonal TAF models described by low axial quadrupole and octupole components that persist over time.

7. Conclusions

We present new paleomagnetic records from Late Pleistocene-Holocene volcanic rocks from southern Colombia. Rock magnetic measurements suggest that magnetite and low-Ti titanomagnetite are the main magnetic carriers with Curie temperatures between 516 and 580 °C. However, thermomagnetic curves also reveal the presence of two magnetic phases and suggest titanomaghemite grains with transitional temperatures between 334 and 433 °C. Magnetic domain structures are compatible with vortex state and multidomain grains.

After applying laboratory procedures and data selection criteria, we obtain high-quality paleodirectional results from 30 sites for the 0–2 Ma age interval for statistical PSV and TAF analyses. The mean direction (Dec = 351.2°, Inc. = −3.4°, α95 = 6.2°, k = 20.0) for these sites does not coincide at the 95% confidence level with directions expected for a GAD field. Similarly, the mean paleomagnetic pole (Plat = 80.7°N, Plon = 173.1°E, A95 = 5.2°, K = 29.1) is statistically different from Earth's spin axis. The VGP dispersion for the 0–2 Ma interval ($S_{B(2Ma)} = 15.2_{12.0}^{17.6°}$) and Brunhes chron normal polarity data ($S_{B(Bru)} = 16.0_{11.6}^{19.1°}$) are statistically compatible within 95% confidence limits with studies at low latitudes and with the predictions of revised PSV models (Model G) for the 0–10 Ma and Brunhes intervals. The high observed VGP scatter in southern Colombia may be associated with anomalous paleodirectional variability over the equatorial Atlantic region influenced by the South Atlantic Magnetic Anomaly that appears to persist on timescales from centuries to millions of years. Further study is needed to test this
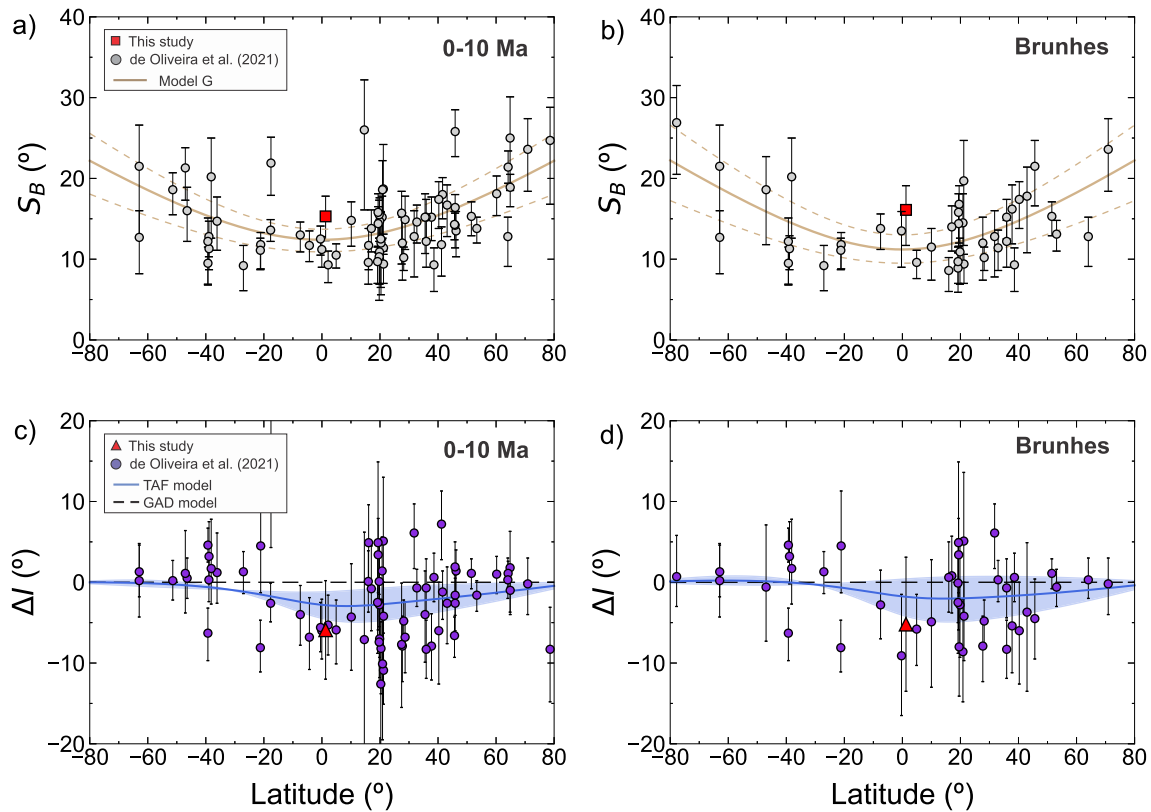
Fig. 7. VGP angular dispersion (S_B) as a function of latitude from this study for the 0–2 Ma period and the Brunhes chron with their 95% bootstrap confidence limits in (a) and (b), respectively, compared to global S_B data (grey circles) for the 0–10 Ma and Brunhes intervals (de Oliveira et al., 2021). Brown lines correspond to Model G curves (McFadden et al., 1988) associated with 95% confidence intervals (brown dashed lines). (c-d) Comparison between inclination anomaly (ΔI) estimates from this study (red triangles) with ΔI data compilations for the last 10 Myr and Brunhes chron (purple circles) in (c) and (d), respectively. Blue curves represent the TAF models (de Oliveira et al., 2021), where blue-shaded areas denote the 95% confidence region. VGP = virtual geomagnetic pole; TAF = time-averaged field. (For interpretation of the references to colour in this figure legend, the reader is referred to the web version of this article.)

Table 3
Selected paleomagnetic studies from −10° to 10° latitude.

Age (Ma)	Slat (°N)	Slon (°E)	Location	N	D (°)	I (°)	α_{95} (°)	S_B (°)	S_{Bl} (°)	S_B^u (°)	ΔI (°)	ΔI_{lo} (°)	ΔI^{up} (°)	Reference
						0–10 Ma interval								
0.005–2.11	10.12	275.48	Costa Rica	29	1.0	15.4	7.1	14.8	11.6	17.1	−4.3	−10.9	2.3	Cromwell et al. (2013)
0–2.65	4.90	284.64	Colombia	42	3.9	3.8	4.3	10.5	8.9	11.9	−5.9	−10.1	−2.2	Sánchez-Duque et al. (2016)
3.53–4.84	2.13	35.77	Loiyangalani, Kenya	31	1.1	−1.0	4.2	9.3	7.1	11.0	−5.3	−9.0	−1.6	Opdyke et al. (2010)
0.5–5.5	−0.04	6.23	Sao Tome Island	38	358.0	−6.1	4.3	11.2	9.0	12.8	−6.0	−9.5	−2.1	Opdyke et al. (2015)
0.0176–2.71	−0.48	281.76	Ecuador	45	0.6	−6.6	4.0	12.5	10.5	14.1	−5.6	−8.6	−2.5	Opdyke et al. (2006)
2.55–10.0	−4.32	327.74	Fernando de Noronha, Brazil	36	358.9	−15.4	4.8	11.7	9.7	13.5	−6.8	−10.8	−1.9	Leonhardt et al. (2003)
0–6.7	−7.46	111.94	Indonesia	44	359.9	−18.7	4.4	13.0	10.9	14.6	−4.0	−7.8	−0.4	Elmaleh et al. (2004)
						Brunhes chron								
0.01–0.50	10.00	275.81	Costa Rica	12	355.9	14.6	9.4	11.5	7.4	13.8	−4.9	−13.0	2.8	Cromwell et al. (2013)
0–0.50	4.91	284.64	Colombia	29	4.1	4.0	4.6	9.6	7.6	11.1	−5.8	−10.3	−1.5	Sánchez-Duque et al. (2016)
0.02–0.45	−0.31	281.79	Ecuador	11	356.4	−9.7	10.0	13.5	9.0	15.9	−9.1	−16.5	−1.5	Opdyke et al. (2006)
0–0.55	−7.52	112.44	Indonesia	36	0.2	−17.6	5.2	13.8	11.2	15.6	−2.8	−7.0	1.5	Elmaleh et al. (2004)

Abbreviations for columns Age to ΔI are as in Table 2. ΔI_{lo} and ΔI^{up} are the lower and upper 95% confidence limits of the inclination anomaly; Reference corresponds to the paleomagnetic study.

hypothesis. Inclination anomalies for each age group ($\Delta I_{2Ma} = -5.9^{0.3^\circ}_{-12.1}$ for the 0–2.0 Ma period and $\Delta I_{Bru} = -5.3^{3.1^\circ}_{-13.7}$ for the Brunhes chron) suggest large negative inclination anomalies observed in global compilations and TAF models with low zonal quadrupole (~3%) and octupole (~1%) contributions superimposed on the axial dipole component. Therefore, our new paleomagnetic results from southern Colombia expand the 0–10 Ma database at equatorial latitudes, with the potential to be used for further investigations of paleomagnetic field structure.

Supplementary data to this article can be found online at https://doi.org/10.1016/j.pepi.2022.106926.

Declaration of Competing Interest

The authors declare that they have no known competing financial interests or personal relationships that could have appeared to influence the work reported in this paper.

Acknowledgments

References

Aldana, M., Costanzo-Álvarez, V., Gómez, L., González, C., Díaz, M., Silva, P., Rada, M., 2011. Identification of magnetic minerals related to hydrocarbon authigenesis in Venezuelan oil fields using an alternative decomposition of isothermal remanence curves. Stud. Geophys. Geod. 55 (2), 343–358. https://doi.org/10.1007/s11200-011-0019-0.

Argus, D.F., Gordon, R.G., DeMets, C., 2011. Geologically current motion of 56 plates relative to the no-net-rotation reference frame. Geochem. Geophys. Geosyst. 12 (11) https://doi.org/10.1029/2011GC003751.

Aubert, J., Finlay, C.C., Fournier, A., 2013. Bottom-up control of geomagnetic secular variation by the Earth's inner core. Nature 502 (7470), 219–223. https://doi.org/10.1038/nature12574.

Banerjee, A., Dhillon, I., Ghosh, J., Sra, S., 2005. Clustering on the unit hypersphere using von Mises-Fisher distributions. J. Mach. Learn. Res. 6, 1345–1382.

Bayona, G.A., García, D.F., Mora, G., 1994. La Formación Saldaña: Producto de la Actividad de Estratovolcanes Continentales en un Dominio de Retroarco. Bogotá D.C. Estudios Geológicos del Valle Superior del Magdalena I, vol. 1, p. 21.

Bayona, G., Bustamante, C., Nova, G., Salazar Franco, A.M., 2020. Jurassic evolution of the northwestern corner of Gondwana: Present knowledge and future challenges in studying Colombian Jurassic rocks. In: Gómez, J., Pinilla Pachon, A.O. (Eds.), The Geology of Colombia - Mesozoic. Servicio Geológico Colombiano, 2. Publicaciones Geológicas Especiales (36, 37 p).

Biggin, A.J., Van Hinsbergen, D.J., Langereis, C.G., Straathof, G.B., Deenen, M.H.L., 2008. Geomagnetic secular variation in the Cretaceous Normal Superchron and in the Jurassic. Phys. Earth Planet. Inter. 169 (1–4), 3–19. https://doi.org/10.1016/j.pepi.2008.07.004.

Biggin, A., Bono, R., Meduri, D.G., Sprain, C., Davies, C.J., Holme, R., Doubrovine, P., 2020. Quantitative estimates of average geomagnetic axial dipole dominance in deep geological time. Nat. Commun. 11 (1), 1–9. https://doi.org/10.1038/s41467-020-19794-7.

Bono, R.K., Biggin, A.J., Holme, R., Davies, C.J., Meduri, D.G., Bestard, J., 2020. Covariant giant Gaussian process models with improved reproduction of palaeosecular variation. Geochem. Geophys. Geosyst. 21 (8) https://doi.org/10.1029/2020GC008960.

Brandt, D., Constable, C., Ernesto, M., 2020. Giant Gaussian process models of geomagnetic paleosecular variation: a directional outlook. Geophys. J. Int. 22 (3), 1526–1541. https://doi.org/10.1093/gji/ggaa258.

Bustamante, C., Archanjo, C.J., Cardona, A., Vervoort, J.D., 2016. Late Jurassic to early Cretaceous plutonism in the Colombian Andes: a record of long-term arc maturity. Bulletin 128 (11–12), 1762–1779. https://doi.org/10.1130/B31307.1.

Calvache, M.L., Duque-Trujillo, J.F., 2016. Geomorphological Features of the Galeras Volcanic Complex. In Landscapes and Landforms of Colombia. Springer, Cham, pp. 193–202.

Calvache, M.L., Cortés, G.P., Williams, S.N., 1997. Stratigraphy and chronology of the Galeras volcanic complex, Colombia. J. Volcanol. Geotherm. Res. 77 (1–4), 5–19. https://doi.org/10.1016/S0377-0273(96)00083-2.

Cediel, F., Mojica, J., Macía, C., 1981. Las formaciones Luisa, Payandé y Saldaña sus columnas estratigráficas características. Geología Norandina 3, 11.

Cepeda, H., 1985. Anotaciones acerca de la geología del volcán Galeras (Colombia). In: Memorias del VI Congreso Latinoamericano de Geología, 1.

Cochrane, R., Spikings, R., Gerdes, A., Ulianov, A., Mora, A., Villagómez, D., et al., 2014. Permo-Triassic anatexis, continental rifting and the disassembly of western Pangaea. Lithos 190, 383–402. https://doi.org/10.1016/j.lithos.2013.12.020.

Coe, R.S., Glatzmaier, G.A., 2006. Symmetry and stability of the geomagnetic field. Geophys. Res. Lett. 33 (21) https://doi.org/10.1029/2006GL027903.

Constable, C.G., Parker, R.L., 1988. Statistics of the geomagnetic secular variation for the past 5 m.y. J. Geophys. Res. 93 (B10), 11569–11581. https://doi.org/10.1029/JB093iB10p11569.

Constable, C., Korte, M., Panovska, S., 2016. Persistent high paleosecular variation activity in southern hemisphere for at least 10 000 years. Earth Planet. Sci. Lett. 453, 78–86. https://doi.org/10.1016/j.epsl.2016.08.015.

Cox, A., 1970. Latitude dependence of the angular dispersion of the geomagnetic field. Geophys. J. R. Astron. Soc. 20 (3), 253–269. https://doi.org/10.1111/j.1365-246X.1970.tb06069.x.

Cox, A., 1975. The frequency of geomagnetic reversals and the symmetry of the nondipole field. Rev. Geophys. 13 (3), 35–51. https://doi.org/10.1029/RG013i003p00035.

Cromwell, G., Constable, C.G., Staudigel, H., Tauxe, L., Gans, P., 2013. Revised and updated paleomagnetic results from Costa Rica. Geochem. Geophys. Geosyst. 14 (9), 3379–3388. https://doi.org/10.1002/ggge.20199.

Cromwell, G., Johnson, C.L., Tauxe, L., Constable, C.G., Jarboe, N.A., 2018. PSV10: a global data set for 0–10 Ma time-averaged field and paleosecular variation studies. Geochem. Geophys. Geosyst. 19 (5), 1533–1558. https://doi.org/10.1002/2017GC007318.

Davies, C.J., Constable, C.G., 2014. Insights from geodynamo simulations into long-term geomagnetic field behaviour. Earth Planet. Sci. Lett. 404, 238–249. https://doi.org/10.1016/j.epsl.2014.07.042.

Day, R., Fuller, M., Schmidt, V.A., 1977. Hysteresis properties of titanomagnetites: grain-size and compositional dependence. Phys. Earth Planet. Inter. 13 (4), 260–267. https://doi.org/10.1016/0031-9201(77)90108-X.

de Oliveira, W.P., Franco, D.R., Brandt, D., Ernesto, M., da Ponte Neto, C.F., Zhao, X., et al., 2018. Behavior of the paleosecular variation during the Permian-Carboniferous Reversed Superchron and comparisons to the low reversal frequency intervals since Precambrian times. Geochem. Geophys. Geosyst. 19 (4), 1035–1048. https://doi.org/10.1002/2017GC007262.

de Oliveira, W.P., Hartmann, G.A., Terra-Nova, F., Brandt, D., Biggin, A.J., Engbers, Y.A., et al., 2021. Paleosecular variation and the time-averaged geomagnetic field since 10 Ma. Geochem. Geophys. Geosyst. 22 (10) https://doi.org/10.1029/2021GC010063.

Doubrovine, P.V., Veikkolainen, T., Pesonen, L.J., Piispa, E., Ots, S., Smirnov, A.V., et al., 2019. Latitude dependence of geomagnetic paleosecular variation and its relation to the frequency of magnetic reversals: observations from the Cretaceous and Jurassic. Geochem. Geophys. Geosyst. 20 (3), 1240–1279. https://doi.org/10.1029/2018GC007863.

Dunlop, D.J., Özdemir, Ö., 1997. Rock Magnetism: Fundamentals and Frontiers. Cambridge University.

Duque Trujillo, J.F., Toro Villegas, G.E., Cardona Molina, A., Calvache Velazco, M., 2010. Geología, geocronología y geoquímica del volcán Morasurco, Pasto, Colombia. Boletín de Ciencias de la Tierra 27 (25–3).

Efron, B., Tibshirani, R., 1993. An Introduction to the Bootstrap. Chapman & Hall, New York.

Egli, R., 2021. Magnetic characterization of geologic materials with first-order reversal curves. In: Magnetic Measurement Techniques for Materials Characterization. Springer, Cham, pp. 455–604. https://doi.org/10.1007/978-3-030-70443-8_17.

Elmaleh, A., Valet, J.P., Quidelleur, X., Solihin, A., Bouquerel, H., Tesson, T., et al., 2004. Palaeosecular variation in Java and Bawean Islands (Indonesia) during the Brunhes chron. Geophys. J. Int. 157 (1), 441–454. https://doi.org/10.1111/j.1365-246X.2004.02197.x.

Engbers, Y.A., Grappone, J.M., Mark, D.F., Biggin, A.J., 2022. Low paleointensities and Ar/Ar ages from Saint Helena provide evidence for recurring magnetic field weaknesses in the South Atlantic. J. Geophys. Res. Solid Earth 127 (3). https://doi.org/10.1029/2021JB023358.

Evans, M.E., Heller, F., 2003. Environmental magnetism: principles and applications of enviromagnetics. Elsevier. 86, 31–49.

Fisher, R.A., 1953. Dispersion on a sphere. Proc. R. Soc. Lond. A 217 (1130), 295–305. https://doi.org/10.1098/rspa.1953.0064.

Fisher, N.I., Lewis, T., Embleton, B.J., 1987. Statistical Analysis of Spherical Data. Cambridge University Press.

Franco, D.R., de Oliveira, W.P., de Freitas, F.B.V., Takahashi, D., da Ponte Neto, C.F., Peixoto, I.M.C., 2019. Paleomagnetic evidence for inverse correspondence between the relative contribution of the axial dipole field and CMB heat flux for the past 270 Myr. Sci. Rep. 9 (1), 1–8. https://doi.org/10.1038/s41598-018-36494-x.

Gautam, P., Blaha, U., Appel, E., Neupane, G., 2004. Environmental magnetic approach towards the quantification of pollution in Kathmandu urban area, Nepal. Phys. Chem. Earth Parts A/B/C 29 (13–14), 973–984. https://doi.org/10.1016/j.pce.2004.02.001.

Haag, M., Heller, F., Allenspach, R., Roche, K., 1990. Self-reversal of natural remanent magnetization in andesitic pumice. Phys. Earth Planet. Inter. 65 (1–2), 104–108. https://doi.org/10.1016/0031-9201(90)90079-D.

Handford, B.T., Biggin, A.J., Haldan, M.M., Langereis, C.G., 2021. Analyzing Triassic and Permian geomagnetic paleosecular variation and the implications for ancient field morphology. Geochem. Geophys. Geosyst. 22 (11) https://doi.org/10.1029/2021GC009930.

Harrison, R.J., Feinberg, J.M., 2008. FORCinel: an improved algorithm for calculating first-order reversal curve distributions using locally weighted regression smoothing. Geochem. Geophys. Geosyst. 9 (5) https://doi.org/10.1029/2008GC001987.

Hartmann, G.A., Pacca, I.G., 2009. Time evolution of the South Atlantic magnetic anomaly. An. Acad. Bras. Cienc. 81, 243–255. https://doi.org/10.1590/S0001-37652009000200010.

Heller, F., Carracedo, J.C., Solert, V., 1986. Reversed magnetization in pyroclastics from the 1985 eruption of Nevado del Ruiz, Colombia. Nature 324 (6094), 241–242. https://doi.org/10.1038/324241a0.

Heslop, D., Roberts, A.P., 2020. Uncertainty propagation in hierarchical paleomagnetic reconstructions. J. Geophys. Res. Solid Earth 125 (6). https://doi.org/10.1029/2020JB019488.

Hulot, G., Finlay, C.C., Constable, C.G., Olsen, N., Mandea, M., 2010. The magnetic field of planet Earth. Space Sci. Rev. 152 (1), 159–222. https://doi.org/10.1007/s11214-010-9644-0.

Jaramillo, J.S., Cardona, A., León, S., Valencia, V., Vinasco, C., 2017. Geochemistry and geochronology from Cretaceous magmatic and sedimentary rocks at 6° 35' N, western flank of the central cordillera (Colombian Andes): magmatic record of arc growth and collision. J. S. Am. Earth Sci. 76, 460–481. https://doi.org/10.1016/j.jsames.2017.04.012.

Johnson, C.L., McFadden, P.L., 2015. The time-averaged field and paleosecular variation. In: Kono, M., Schubert, G. (Eds.), Geomagnetism. Treatise on Geophysics, , 2nd edvol. 5. Elsevier, pp. 385–417. https://doi.org/10.1016/b978-0-444-53802-4.00105-6.

Johnson, C.L., Constable, C.G., Tauxe, L., Barendregt, R., Brown, L.L., Coe, R.S., et al., 2008. Recent investigations of the 0–5 Ma geomagnetic field recorded by lava flows. Geochem. Geophys. Geosyst. 9 (4) https://doi.org/10.1029/2007GC001696.

Kerr, A.C., Tarney, J., Marriner, G.F., Nivia, A., Klaver, G.T., Saunders, A.D., 1996. The geochemistry and tectonic setting of late Cretaceous Caribbean and Colombian volcanism. J. S. Am. Earth Sci. 9 (1–2), 111–120. https://doi.org/10.1016/0895-9811(96)00031-4.

Kirschvink, J.L., 1980. The least-squares line and plane and the analysis of palaeomagnetic data. Geophys. J. R. Astron. Soc. 62, 699–718. https://doi.org/10.1111/j.1365-246X.1980.tb02601.x.

Laj, C., Channell, J.E., 2015. Geomagnetic excursions. In: Kono, M. (Ed.), Geomagnetism; Schubert, G. (Ed.), Treatise on Geophysics, , 2nd ed.5. Elsevier, Amsterdam, The Netherlands, pp. 343–383.

Lascu, I., Einsle, J.F., Ball, M.R., Harrison, R.J., 2018. The vortex state in geologic materials: a micromagnetic perspective. J. Geophys. Res. Solid Earth 123 (9), 7285–7304. https://doi.org/10.1029/2018JB015909.

Lattard, D., Engelmann, R., Kontny, A., Sauerzapf, U., 2006. Curie temperatures of synthetic titanomagnetites in the Fe-Ti-O system: effects of composition, crystal chemistry, and thermomagnetic methods. J. Geophys. Res. Solid Earth 111 (B12). https://doi.org/10.1029/2006JB004591.

Leonhardt, R., Matzka, J., Menor, E.A., 2003. Absolute paleointensities and paleodirections of Miocene and Pliocene lavas from Fernando de Noronha, Brazil. Phys. Earth Planet. Inter. 139 (3–4), 285–303. https://doi.org/10.1016/j.pepi.2003.09.008.

Lhuillier, F., Hulot, G., Gallet, Y., 2013. Statistical properties of reversals and chrons in numerical dynamos and implications for the geodynamo. Phys. Earth Planet. Inter. 220, 19–36. https://doi.org/10.1016/j.pepi.2013.04.005.

McCourt, W.J., Aspden, J.A., Brook, M., 1984. New geological and geochronological data from the Colombian Andes: continental growth by multiple accretion. J. Geol. Soc. 141 (5), 831–845. https://doi.org/10.1144/gsjgs.141.5.0831.

McElhinny, M.W., McFadden, P.L., Merrill, R.T., 1996. The time-averaged paleomagnetic field 0–5 Ma. J. Geophys. Res. 101 (B11), 25007–25027. https://doi.org/10.1029/96JB01911.

McFadden, P.L., Merrill, R.T., McElhinny, M.W., 1988. Dipole/quadrupole family modeling of paleosecular variation. J. Geophys. Res. 93 (B10), 11583–11588. https://doi.org/10.1029/JB093iB10p11583.

Merrill, R.T., McFadden, P.L., 2003. The geomagnetic axial dipole field assumption. Phys. Earth Planet. Inter. 139 (3–4), 171–185. https://doi.org/10.1016/j.pepi.2003.07.016.

Mojica, J., 1980. Observaciones acerca del estado actual del conocimiento de la Formación Payandé (Triásico Superior), Valle Superior del río Magdalena, Colombia. Geología Colombiana 11, 67–88.

Mojica, J., Prinz-Grimm, P., 2000. La fauna de amonitas del Triásico Tardío en el Miembro Chicalá (parte baja de la Formación Saldaña) en Payandé, Tolima, Colombia. Geología Colombiana 25, 13–23.

Monsalve Bustamante, M.L., 2020. The volcanic front in Colombia: segmentation and recent and historical activity. Geol. Colombia 4, 97–159.

Montes, C., Rodriguez-Corcho, A.F., Bayona, G., Hoyos, N., Zapata, S., Cardona, A., 2019. Continental margin response to multiple arc-continent collisions: the northern Andes-Caribbean margin. Earth Sci. Rev. 198, 102903 https://doi.org/10.1016/j.earscirev.2019.102903.

Ogg, J.G., 2020. Geomagnetic polarity time scale. In: Geologic Time Scale 2020. Elsevier, pp. 159–192.

Opdyke, N.D., Hall, M., Mejia, V., Huang, K., Foster, D.A., 2006. Time-averaged field at the equator: results from Ecuador. Geochem. Geophys. Geosyst. 7 (11) https://doi.org/10.1029/2005GC001221.

Opdyke, N.D., Kent, D.V., Huang, K., Foster, D.A., Patel, J.P., 2010. Equatorial paleomagnetic time-averaged field results from 0–5 Ma lavas from Kenya and the latitudinal variation of angular dispersion. Geochem. Geophys. Geosyst. 11 (5) https://doi.org/10.1029/2009GC002863.

Opdyke, N.D., Kent, D.V., Foster, D.A., Huang, K., 2015. Paleomagnetism of Miocene volcanics on Sao Tome: paleosecular variation at the equator and a comparison to its

latitudinal dependence over the last 5 Myr. Geochem. Geophys. Geosyst. 16 (11), 3870–3882. https://doi.org/10.1002/2015GC005901.

Panovska, S., Constable, C.G., 2017. An activity index for geomagnetic paleosecular variation, excursions, and reversals. Geochem. Geophys. Geosyst. 18 (4), 1366–1375. https://doi.org/10.1002/2016GC006668.

Panovska, S., Constable, C.G., Korte, M., 2018. Extending global continuous geomagnetic field reconstructions on timescales beyond human civilization. Geochem. Geophys. Geosyst. 19 (12), 4757–4772. https://doi.org/10.1029/2018GC007966.

Panovska, S., Korte, M., Constable, C.G., 2019. One hundred thousand years of geomagnetic field evolution. Rev. Geophys. 57 (4), 1289–1337. https://doi.org/10.1029/2019RG000656.

Pardo, N., Pulgarín, B., Betancourt, V., Lucchi, F., Valencia, L.J., 2019. Facing geological mapping at low-latitude volcanoes: the Doña Juana volcanic complex study-case, SW-Colombia. J. Volcanol. Geotherm. Res. 385, 46–67. https://doi.org/10.1016/j.jvolgeores.2018.04.016.

Pindell, J.L., Kennan, L., 2009. Tectonic evolution of the Gulf of Mexico, Caribbean and northern South America in the mantle reference frame: an update. Geol. Soc. Lond., Spec. Publ. 328 (1), 1–55. https://doi.org/10.1144/SP328.1.

Ramos, V.A., 2009. Anatomy and Global Context of the Andes: Main Geologic Features and the Andean Orogenic Cycle. Backbone of the Americas: Shallow Subduction, Plateau Uplift, and Ridge and Terrane Collision, 204, pp. 31–65.

Roberts, A.P., Pike, C.R., Verosub, K.L., 2000. First-order reversal curve diagrams: a new tool for characterizing the magnetic properties of natural samples. J. Geophys. Res. Solid Earth 105 (B12), 28461–28475. https://doi.org/10.1029/2000JB900326.

Roberts, A.P., Heslop, D., Zhao, X., Pike, C.R., 2014. Understanding fine magnetic particle systems through use of first-order reversal curve diagrams. Rev. Geophys. 52 (4), 557–602. https://doi.org/10.1002/2014RG000462.

Roberts, A.P., Almeida, T.P., Church, N.S., Harrison, R.J., Heslop, D., Li, Y., et al., 2017. Resolving the origin of pseudo-single domain magnetic behavior. J. Geophys. Res. Solid Earth 122 (12), 9534–9558. https://doi.org/10.1002/2017JB014860.

Roberts, A.P., Tauxe, L., Heslop, D., Zhao, X., Jiang, Z., 2018. A critical appraisal of the "Day" diagram. J. Geophys. Res. Solid Earth 123 (4), 2618–2644. https://doi.org/10.1002/2017JB015247.

Rodríguez, G., Arango, M.I., Zapata, G., Bermúdez, J.G., 2018. Petrotectonic characteristics, geochemistry, and U-Pb geochronology of Jurassic plutons in the upper Magdalena Valley-Colombia: implications on the evolution of magmatic arcs in the NW Andes. J. S. Am. Earth Sci. 81, 10–30. https://doi.org/10.1016/j.jsames.2017.10.012.

Rother, M., Korte, M., Morschhauser, A., Vervelidou, F., Matzka, J., Stolle, C., 2021. The Mag.Num core field model as a parent for IGRF-13, and the recent evolution of the South Atlantic anomaly. Earth Planets Space 73 (1), 1–17. https://doi.org/10.1186/s40623-020-01277-0.

Salminen, J., Pesonen, L.J., 2007. Paleomagnetic and rock magnetic study of the Mesoproterozoic sill, Valaam island, Russian Karelia. Precambrian Res. 159 (3–4), 212–230. https://doi.org/10.1016/j.precamres.2007.06.009.

Sánchez-Duque, A., Mejia, V., Opdyke, N.D., Huang, K., Rosales-Rivera, A., 2016. Plio-Pleistocene paleomagnetic secular variation and time-averaged field: Ruiz-Tolima volcanic chain, Colombia. Geochem. Geophys. Geosyst. 17 (2), 538–549. https://doi.org/10.1002/2015GC006149.

Spikings, R., Cochrane, R., Villagomez, D., Van der Lelij, R., Vallejo, C., Winkler, W., Beate, B., 2015. The geological history of northwestern South America: from Pangaea to the early collision of the Caribbean large Igneous Province (290–75 Ma). Gondwana Res. 27 (1), 95–139. https://doi.org/10.1016/j.gr.2014.06.004.

Sprain, C.J., Biggin, A.J., Davies, C.J., Bono, R.K., Meduri, D.G., 2019. An assessment of long duration geodynamo simulations using new paleomagnetic modeling criteria (QPM). Earth Planet. Sci. Lett. 526, 115758 https://doi.org/10.1016/j.epsl.2019.115758.

Taboada, A., Rivera, L.A., Fuenzalida, A., Cisternas, A., Philip, H., Bijwaard, H., et al., 2000. Geodynamics of the northern Andes: subductions and intracontinental deformation (Colombia). Tectonics 19 (5), 787–813. https://doi.org/10.1029/2000TC900004.

Tarduno, J.A., Watkeys, M.K., Huffman, T.N., Cottrell, R.D., Blackman, E.G., Wendt, A., et al., 2015. Antiquity of the South Atlantic anomaly and evidence for top-down control on the geodynamo. Nat. Commun. 6 (1), 1–6. https://doi.org/10.1038/ncomms8865.

Tauxe, L., 2003. Paleomagnetic Principles and Practice, vol. 18. Kluwer Academic Publishers.

Tauxe, L., 2010. Essentials of Paleomagnetism. University of California Press.

Tauxe, L., Kent, D.V., 2004. A simplified statistical model for the geomagnetic field and the detection of shallow bias in paleomagnetic inclinations: Was the ancient magnetic field dipolar? In: Channell, J.E.T., Kent, D.V., Lowrie, W., Meert, J.G. (Eds.), Timescales of the Paleomagnetic Field. American Geophysical Union, pp. 101–115. https://doi.org/10.1029/145GM08.

Terra-Nova, F., Amit, H., Choblet, G., 2019. Preferred locations of weak surface field in numerical dynamos with heterogeneous core–mantle boundary heat flux: consequences for the South Atlantic anomaly. Geophys. J. Int. 217 (2), 1179–1199. https://doi.org/10.1093/gji/ggy519.

Vandamme, D., 1994. A new method to determine paleosecular variation. Phys. Earth Planet. Inter. 85 (1–2), 131–142. https://doi.org/10.1016/0031-9201(94)90012-4.

Veikkolainen, T., Pesonen, L.J., 2014. Palaeosecular variation, field reversals and the stability of the geodynamo in the Precambrian. Geophys. J. Int. 199 (3), 1515–1526. https://doi.org/10.1093/gji/ggu348.

Villagómez, D., Spikings, R., Magna, T., Kammer, A., Winkler, W., Beltrán, A., 2011. Geochronology, geochemistry and tectonic evolution of the Western and central cordilleras of Colombia. Lithos 125 (3–4), 875–896. https://doi.org/10.1016/j.lithos.2011.05.003.

Wagner, L.S., Jaramillo, J.S., Ramírez-Hoyos, L.F., Monsalve, G., Cardona, A., Becker, T. W., 2017. Transient slab flattening beneath Colombia. Geophys. Res. Lett. 44 (13), 6616–6623. https://doi.org/10.1002/2017GL073981.

Zapata, S., Cardona, A., Jaramillo, C., Valencia, V., Vervoort, J., 2016. U-Pb LA-ICP-MS geochronology and geochemistry of Jurassic volcanic and plutonic rocks from the Putumayo region (southern Colombia): tectonic setting and regional correlations. Boletín de Geología 38 (2), 21–38. https://doi.org/10.18273/revbol.v38n2-2016001.

Zapata, S., Cardona, A., Jaramillo, J.S., Patiño, A., Valencia, V., León, S., et al., 2019. Cretaceous extensional and compressional tectonics in the northwestern Andes, prior to the collision with the Caribbean oceanic plateau. Gondwana Res. 66, 207–226. https://doi.org/10.1016/j.gr.2018.10.008.

Zhao, X., Roberts, A.P., Heslop, D., Paterson, G.A., Li, Y., Li, J., 2017. Magnetic domain state diagnosis using hysteresis reversal curves. J. Geophys. Res. Solid Earth 122 (7), 4767–4789. https://doi.org/10.1002/2016JB013683.

Zijderveld, J.D.A., 1967. AC demagnetization of rocks: Analysis of results. In: Collinson, D.W., Creer, K.M., Runcorn, S.K. (Eds.), Methods in Palaeomagnetism. Elsevier, Amsterdam.